Nanoparticle-Induced Radial Structural Gradients in Melt-Spun Polypropylene/PPgMA Fibers

J. H. Fujiyama-Novak and M. Cakmak*

Polymer Engineering Institute, University of Akron, Akron, Ohio 44325-0301

Received August 15, 2007; Revised Manuscript Received June 11, 2008

ABSTRACT: The presence of nanoparticles on the evolution of structural hierarchy in both highly anisotropic clay phase and polymer phase in melt-spun PP/PPgMA (maleic anhydride-modified polypropylene) fibers was investigated. The melt stream that exits the die was found to contain orientation gradient in the radial direction that is preserved even after solidification without application of a takeup. This is due to the influence of shearing in the die that results in a band of oriented outer layers where broad surfaces of the clay particles become parallel to the surface of the fibers. The polymer phase trapped between these particles exhibits moderate to high preferrential orientation levels. The interior of the fibers was found to exhibit low levels of preferred orientation in both the clay and the polymer phases. Upon application of takeup, the presence of clay particles substantially enhances the orientation of amorphous and crystalline phases in PP/PPgMA fibers. This is due to the substantial decrease in chain relaxation in the proximity of the clay platelets and enhancement of orientation in the polymer phase in the vicinity of particles that create amplified deformation field by their relative motions. Measurements of the clay orientation in the melt-spun fibers as they undergo "confined melting" in constrained state revealed that these naturally anisotropic nanoplatelets contribute positively to the birefringence of the fibers.

Introduction

In the fiber spinning process, the type of deformation in the major part of the spin line is uniaxial extension[1] though the material that comes out of the die has just undergone substantial shearing. In a one-step melt spinning, drawing of molten polymer jet into thin fiber form occurs under high-stress conditions while rapid cooling solidifies the fiber into final shape.

Basic studies of the structure of isotactic polypropylene fibers have been carried out by Katayama et al.,[2] Kitao et al.,[3] Shimizu and Shimazaki,[4] and many others. These authors reported that rapid cooling leads to mesomorphic structure called smectic while moderate to high speeds yield fibers exhibiting monoclinic structures. In a narrower window, crystallization that takes place at moderate cooling and low stresses may also yield hexagonal crystal structure formation that typically occurs at crystallization temperatures in the 120−140 °C range.[5] Spruiell and White,[6] Ishizuka and Koyama,[7] and Nadella et al.[8] showed that the chain axis crystalline orientation factors for melt-spun monofilaments increased with the takeup speed, and these orientation factor studies with different molecular weight resins were found to collapse into one master nonlinear curve when correlated with spin-line stress. In addition, these fibers may exhibit bimodal orientation: One population, characterized as *a** orientated population where the basal plane (*a*−*b* crystallographic plane) of the lamellae makes about 80° to basal plane of the other population with *c*-axes preferrentially oriented along the fiber axis. The signature for the presence of *a** oriented population is the appearance of off-equatorial (near meridional) appearance of (110) plane population. The second population is called *c*-axis oriented population with the chain axes primarily oriented along the fiber axis.

There have been several reports on the preparation of a PP/clay nanocomposites, specifically, the morphology[9] of the reinforced resin in compression-molded form, their properties,[10−12] and rheological characteristics.[13] In nanoclay reinforced polymers, nanoparticles substantially enhance modulus.[14] The amount of compatibilizer, maleic anhydride-modified PP, helps to increase intercalation, and/or favor exfoliation also enhances the modulus.

Zhang et al.[15] prepared PP/OMMT hybrid fibers and observed that the nanolayered silicates were dispersed in the PP resin at the nanometer level but agglomerated during the process of melt spinning. Pavlkova et al.[16] showed by TEM that the draw down ratio of the fibers increases the level of exfoliation and orientation of the clay, i.e., fluorine-containing hectorite. Mlynarcikova et al.[17] showed that clay platelets orient parallel to the surface of a spun fiber of syndiotactic polypropylene/clay nanocomposite during melt spinning using TEM study. However, their study did not include the details on effect of processing conditions on this orientation behavior and its possible distribution in the radial direction and polymer matrix orientation.

As mentioned earlier, the development of preferrential orientation of polymer chains in the fiber spinning process is well understood. However, there has not been any significant study on the quantitative evaluation of spatial arrangements nanoparticles and polymer (crystalline and amorphous) phases in the isotactic PP fibers. For example, it is not clear how the nanoplatelets under the shear and extensional flows typical of melt spinning behave and how they ultimately influence the orientation and crystallization behavior of polymer chains in their neighborhood.

To answer these questions, in this paper, we focus on three-dimensional dispersion and orientation of the clay particles by WAXS, SAXS, TEM, and AFM techniques. In order to quantify the birefringence contribution from clay particles, a special series of "confined melting" studies were carried out while the birefringence data were acquired. Finally, with these results we will propose a mechanistic model that explains the structural hierarchy in these fibers.

Experimental Section

Materials. The polymers used for the preparation of the nanocomposites are commercial polypropylene PP (Exxon-Mobil-PP4772) and the maleic anhydride-modified polypropylene, PPgMA (Exxon

* To whom correspondence should be addressed.

10.1021/ma8007527 CCC: $40.75
Published on Web 08/08/2008

Table 1. Molecular Weight of PP and PPgMA

material	MFR (g/10min)[a]	M_n	M_w	M_z
PPgMA	27	60 000	100 400	159 900
PP	1.6	113 400	342 500	790 100

[a] 230 °C/2.16 kg.

Mobil-PO1015), with 0.4% of maleic anhydride. The molecular weight information on both polymers is given in Table 1.

Cloisite 20A from Southern Clay Products was used for this study. This is a dimethyl, dehydrogenated tallow quaternary ammonium modified clay with a basal spacing of 24.2 Å.

Mixing. PP, PPgMA, and clay and were dried at 80 °C in vacuum for 12 h. In this work we used a two-step melt mixing strategy to improve the dispersion of fillers. In the first step a masterbatch 25 wt % of clay in PPgMA was prepared in a Leistrich counter-rotating twin-screw extruder operating at 180 °C at 100 rpm. In the second step the PPgMA/clay masterbatch was then diluted to attain right proportion of PP and PPgMA using a twin-screw extruder with melt temperature set at 200 °C. After dilution, all the samples had 15 wt % PPgMA. In the final stage we obtain compounds containing clay loading of 1, 3, and 5 wt % in PP/PPgMA matrix.

Melt Spinning. The samples containing PP, PP/PPgMA, and PP/PPgMA/clay were melt-spun as monofilament through a capillary die (diameter 1.6 mm and length-to-diameter ratio 28) using a capillary rheometer (Instron) and a takeup device. The rheometry temperature was kept at 200 °C. In addition to producing gravity-spun fibers with no takeup application, we produced spun fibers through ambient air cooling at various draw-down ratios (DDR = D_{die}^2/D_{fiber}^2) ranging from 50 to 1000. Here D_{die} and D_{fiber} are the die and the fiber diameters, respectively.

Wide-Angle X-ray Diffraction and Crystalline Orientation. Wide-angle X-ray scattering diffractometer scanning ($2\theta/\theta$ reflection mode) was performed using a Rigaku RU-200B operated at 40 kV and 150 mA. The X-ray beam was nickel-filtered Cu Kα_1 (λ = 0.1504 nm) radiation, and the clay dispersion data were collected from 1.5° to 10° 2θ. To measure the crystalline orientation, a Bruker 8 Discovery was operated at 40 kV and 40 mA with Cu target. The crystalline chain orientation factors were determined from azimuthal distribution of (110) and (040) intensities corrected for the amorphous background using the following equation.[18]

$$\langle \cos^2 \chi_{hkl} \rangle = \frac{\int_0^{\pi/2} I(\chi) \sin \chi \cos^2 \chi \, d\chi}{\int_0^{\pi/2} I(\chi) \sin \chi \, d\chi} \quad (1)$$

$$\langle \cos^2 \chi_{c,Z} \rangle = 1 - 1.099 \langle \cos^2 \chi_{110,Z} \rangle - 0.901 \langle \cos^2 \chi_{040,Z} \rangle \quad (2)$$

The *b*-axis orientation was directly calculated from the experimental $\langle \cos^2 \chi_{040,Z} \rangle$ value using[20]

$$f_b = \frac{3\langle \cos^2 \chi_{040,Z} \rangle - 1}{2} \quad (3)$$

Similarly f_c was determined, and the f_a was extracted from

$$f_a + f_b + f_c = 0 \quad (4)$$

A special microbeam WAXS camera developed to investigate the structural gradients typical of injection molding was used to obtain WAXS patterns at a series of locations in the radial direction on selected samples. This camera has precision sample positioning device that allows probing of the samples at desired increments. The pinhole collimation generated 100 μm diameter beam at the sample position. The beam was monochromatized using a nickel filter.

Birefringence. Birefringence (Δn_{12}) of solid fibers was measured using a polarized light microscope equipped with 4 and 30 order Berek compensators. In order to find out the contribution of clay particles on the overall birefringence of the final fibers, we embedded selected fibers in a high-temperature epoxy sandwiched between two cover glass plates and allowed them to solidify overnight. These fibers were then placed on a Mettler hot stage, and temperature was raised at stepwise 5 deg increments from room temperature followed by short equilibrium time. Following this equilibrium stage, we measured the birefringence of the fibers that are completely surrounded by optically isotropic epoxy medium. These measurements were carried out well into the molten state. By embedding the fibers in epoxy, we were able to prevent any type of flow or deformation as the PP phase melts away, thereby minimizing any structural, particularly clay particle, rearrangement. This then allowed us to carry out complete melting of PP phase while continuing to measure the residual birefringence directly attributable to the clay particles. The birefringence of the molten fibers was determined by normalizing the optical path with the fraction of birefringent material present in the fiber assuming the nanofillers have a specific gravity of 1.77,[19] and therefore the amount of filler in the PP/PPgMA/clay 5 wt % is equal to 2.5 vol %.

The amorphous birefringence of unfilled PP/PPgMA fibers (f_a) were determined from the measured birefringence and crystalline orientation factors (f_c) obtained from WAXS patterns using the ideal two-phase model[20] assuming no form birefringence.

$$\Delta n = X f_c \Delta_c^\circ + (1 - X) f_a \Delta_a^\circ + \Delta n_{form} \quad (5)$$

In this expression we used DSC measured crystallinity (X) and Δ_c° (0.029) and Δ_a° (0.060) for intrinsic birefringences of crystalline and amorphous phase.[21]

For nanoparticle filled systems, we were able to subtract the contribution of the clay particles and applied the above equation.

Thermal Analysis. The thermal behavior of the samples of about 3 mg that were crimped in aluminum pans was investigated using a differential scanning calorimeter (DSC, Perkin-Elmer DSC-7) purged with nitrogen. The experiments were heated with a constant heating rate of 10 °C min from 25 to 230 °C.

Crystallinity (X_c) is obtained using the equation after normalizing the experimentally determined heat of fusion data for the total mass of the polymer present.

$$X_c\,(\%) = \Delta H_{EXP}/\Delta H^\circ$$

$$\Delta H^\circ = 209 \text{ J/g}^{22} \quad (6)$$

Transmission Electron Microscopy. TEM measurements were carried out with a transmission electron microscope applying an acceleration voltage of 120 kV. The specimens were prepared by embedding the fibers in "LR white" embedding media and sectioned with an ultramicrotome at −80 °C using a diamond knife.

Scanning Electron Microscopy. The fibers were coated with a silver target for 45 s and 30 mA current using a K575 Turbo sputter coater (Emitech). A Hitachi S-2150 SEM microscope was used to obtain surface images at 5000× magnification.

Atomic Force Microscopy (AFM). A Digital Instruments Nanoscope IIIa multimode scanning probe microscope was used in the tapping mode with an uncoated silicon probe (resonance frequency 60−80 kHz). The samples were not subjected to pretreatment, and height and phase measurements were obtained using vertical track of the image coincident with the spinning direction of the fiber. All samples were analyzed at room temperature.

Results

Intercalation Effect of PPgMA in PP/Clay System. One of the most important structural features of the nanocomposites is the degree of intercalation/exfoliation of the nanoplatelets in the polymer matrix. The increases in exfoliation lead to generation of large interface between the soft polymer phase and the hard nanoplatelets. As a consequence, the fraction of these rigid particles that is needed to obtain the same effect in properties including rheology (Lee and Han[23]) and structural evolution (Yalcin et al.,[24,25] Ergungor et al.[26]) decreases as the exfoliation increases. The direct evidence of the intercalation is provided by the wide-angle X-ray diffraction scans in the 0.5−10° 2θ range. Figure 1 shows the X-ray analysis of PP/

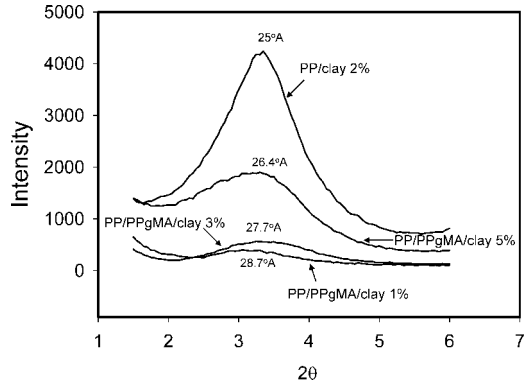

Figure 1. Wide-angle X-ray diffractogram of PP/clay and PP/PPgMA/clay with different filler concentrations.

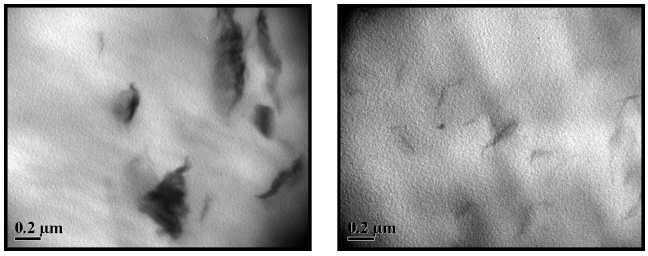

Figure 2. TEM micrographs of (a) PP/2% clay and (b) PP/PPgMA/3% clay.

clay and PP/PPgMA blends containing varied clay content levels ranging from 1 to 5 wt %. To illustrate the improvement of intercalation and exfoliation of the clay in PP in the presence of compatibilizer PPgMA, a binary sample of PP with 2 wt % of Cloisite 20A in PP was also prepared and characterized. As can be observed, the (001) peak for the latter binary blend shows the smallest spacing, and the presence of PPgMA enhances the ability to penetrate into the galleries of the clay particles as evidenced by the increase of this spacing up to 29 Å though at 5% this spacing reduces to 26 Å. Therefore, the sample with lower clay content (1 wt %) showed the highest state of intercalation. As mentioned earlier, in our preparation protocol, we utilized a two-step process: In the first step, we prepared PPgMA + clay masterbatches to make sure that the maleic anhydride-modified PP is well dispersed within the clay. We expect that these PPgMA chains ultimately remain in close proximity with the clay particles, ensuring their penetration within the galleries of the clay particles as the unmodified PP has little to no interaction. This was experimentally shown in the binary system above. In the second stage PP and additional PPgMA were added to obtain the desired composition.

The evidence of nanoplatelet dispersion in the PP/PPgMA matrix is also shown in Figure 2. The TEM micrographs at a magnification of 37 000× are presented in parts a and b of Figure 2 for the PP/clay 2 wt % and PP/PPgMA/clay 3 wt % composites, respectively. The PP/clay system shows large tactoids in accordance with the X-ray results in spite of the lower percentage of loading. This is because Cloisite 20A clay and polypropylene lack compatibility. PPgMA that acts as a compatibilizer improves the dispersion of clay in the polypropylene. On the basis of these results, we conclude that the PP/PPgMA/clay nanocomposites are mostly intercalated and partially exfoliated as evidenced by the TEM. The latter also shows that these particles are dispersed well in the polymer matrix.

In order to eliminate the contribution from the downstream extensional forces, we extruded samples through the capillary die without takeup. In this mode of processing, other than minimal gravitational forces, there were no externally applied

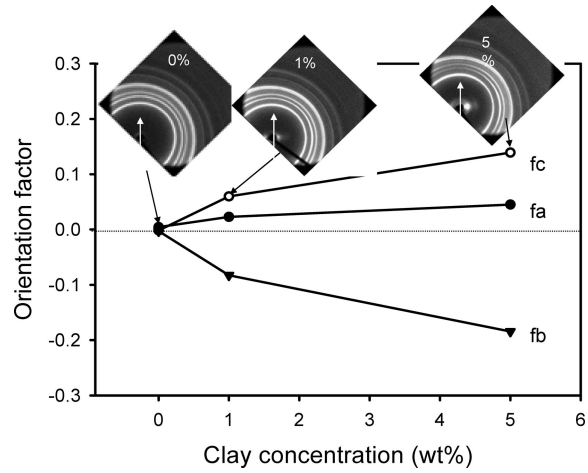

Figure 3. Crystalline orientation factor of PP vs clay % of PP/PPgMA/clay fiber with no takeup.

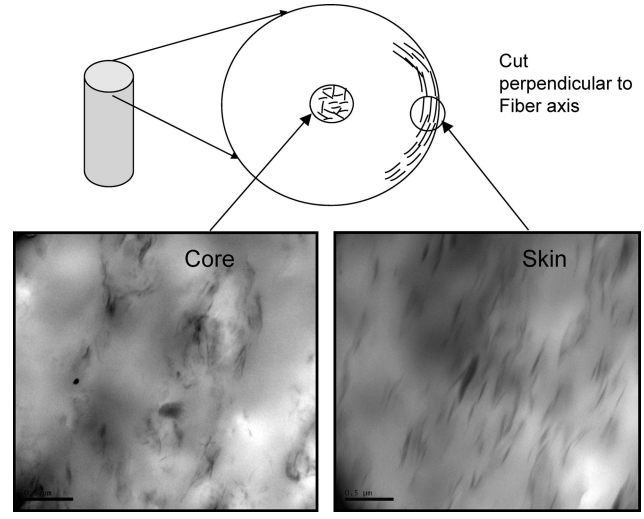

Figure 4. TEM micrographs of PP/PPMA/clay 5% fiber with DDR = 1.

extensional forces prior to freezing of the sample. Figure 3 shows the WAXS patterns together with the quantitative analysis of the crystalline orientation factors of the as-extruded fibers. The unfilled PP/PPgMA monofilament exhibits no orientation as expected. With the addition of clay, the orientation factor of *a* and those of *c* axes show appreciable values. Further increase of clay concentration to 5% increases the magnitude of latter orientation factors. These observations are unusual and raise the question of what is the role of nanoclay on the observed preferential orientation of the polymer chains in these fibers obtained without application of any extensional forces. To elucidate this, TEM and SAXS analyses of PP/PPgMA and PP/PPgMA/clay threads were performed as described below.

Nanoparticle Orientation in Fiber under Influence of Shear Forces. Transmission electron microscopy is well suited to spatially localize the dispersion and orientation information on the clay particles in the polymer matrix. This technique is particularly useful in examining the behavior of fully exfoliated clay platelets that the WAXS technique is relatively insensitive to. Figure 4 shows the cut schematic and the TEM pictures of the PP/PPgMA/clay 5 wt % fiber with DDR = 1 (no takeup) to investigate the orientation behavior of the clay in the fiber without the influence of external extensional forces.

Two samples for TEM samples were cryogenically cut perpendicular to the fiber axis (A-surface cut): one cut very close

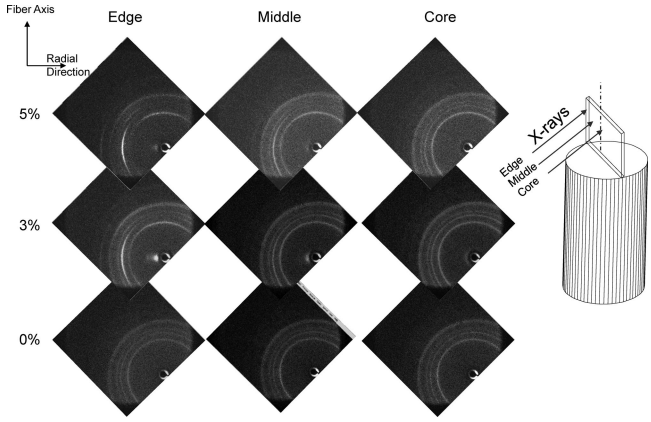

Figure 5. Micro-WAXD patterns of PP/PPgMA extrudates with various clay loadings with no takeup.

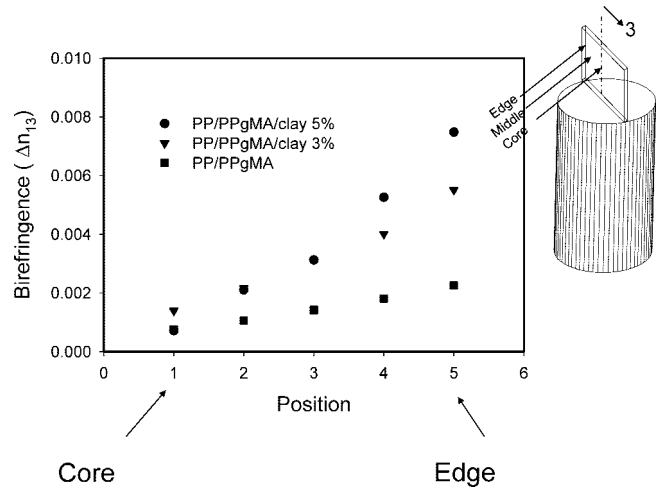

Figure 6. Birefringence (Δn_{12} (1 = fiber direction, 2 = transverse direction) of fibers obtained with no takeup.

to the edge of the fiber (skin) and another was acquired in the center of the fiber (core). The sample thickness was 50−75 nm.

Both micrographs show good distribution of intercalated and exfoliated nanoclay platelets in the polymer matrix. The core sample does not exhibit significant preferrential orientation of clay particles. On the other hand, the sample extracted in the skin region exhibits distinct orientation of the platelets in the hoop direction with the platelet normals pointing in the radial direction, indicating their prealignment has taken place during the flow inside the die and preserved during the exit and subsequently frozen-in upon crystallization.

To further unravel the structural hierarchy that varies in the radial direction in the undrawn fibers, we microtomed the monofilaments in the midplane parallel to the spinning direction as illustrated in Figure 5. Using a microbeam X-ray camera providing a 100 μm collimated beam, three WAXD patterns were obtained from core to edge of this sample mounted on a precision micrometer-driven platform. For this, the sample was cut into the shape shown in Figure 5 so that a uniform thickness slice passing through the symmetry axis was obtained. Unfilled control sample exhibits no apparent crystalline orientation in all three positions along the radius of the fiber as expected. The core of 3% and 5% filled samples also show random pattern. However, in each of the latter two samples, the highest crystalline orientation in PP phase is observed at the edge. This behavior is in concert with the nanoparticle orientation gradient observed in TEM measurements. To improve the spatial resolution, samples were cut in slices with 200 μm of thickness, and birefringence measurements from core (position 1) to edge (position 5) were determined (Figure 6). Birefringence, a measure of overall orientation and its radial variation, also confirms the highest values in the edge though we observe slight anisotropy even in the unfilled fiber.

The preferrential orientation of clay platelets and polymer chains in the skin and the absence of orientation in the core confirm that nanoplatelets preferrentially oriented parallel to the exterior surfaces near the skin region as they experience the highest stresses near the walls of the die while they are passing through it. What is most remarkable is the presence of orientation in the polymer chains in these samples that have not been mechanically subjected to takeup stresses by an external takeup device. This clearly points that these orientations are developed in between the nanoplatelets as they undergo shearing flow in the passage through the extruder and die, and once oriented in the molten state their relaxation is suppressed due to their proximity to the solid surfaces of the clay particles. Yalcin et al.[24] experimentally described this "shear amplification" effect in great detail in the presence of montmorillonite type clay for injection-molded nylon-6 nanocomposites. In the latter high-shear process, even the core regions were found to be highly oriented in nylon-6 which normally does not exhibit orientation even close to the skin regions due to its naturally low viscosity in the absence of nanoparticles. In the present work, relatively low shear flow velocity of the extrusion employed also clearly promotes such significant levels of orientation. The effect has two parts: (1) amplification or shearing experienced by the polymer chains in the neighborhood of the nanoclay particles and (2) significant reduction in the relaxation of oriented chains by their proximity to solid surfaces of the polymer chains. This in turns leads to the observation of high crystalline orientation without even applying the takeup as in the extruded strands.

Recent numerical simulation study on flow-induced crystallization of polymer filled with rigid particles by Hwang et al.[27]concluded that the presence of particles in polymer melts produce regions with highly oriented polymer chains between the spherical particles that are in close proximity. This is evidenced through mapping of recoverable strain measures maps in the vicinity of these spherical particles. In this simulation study the use of spherical particles results in subdued amplification of strain effect as the gap distance varies between closely positioned spheres. The polymer chains in their vicinity do not experience as pronounced an amplification as in the planar particle case that is reported in this paper. In our case the particles have extremely high aspect ratio plus naturally exhibit stacking parallel to one another with very narrow gaps between them as evidenced by TEM studies. As indicated by TEM results, the spacing between the adjacent nanoparticles are relatively small and uniform. The polymer chains that remain in these spaces are in close proximity of these solid surfaces and are heavily influenced by their presence. Therefore, the extent of relaxation is amplified by the large amount of particle/polymer interfaces generated in this nanoclay−polymer system. This phenomenon is not typical and much less pronounced in polymers filled with rigid macroparticles. For the polymer chains of our system, the level of orientation depends not only on the interparticle distance but also mainly on the level of nanoplatelet orientation and average distance between a polymer chain and nearest solid surface which is substantial.

Thermal Behavior and Crystallization of Spun Fibers. PP/PPgMA and PP/PPgMA/clay nanocomposite fibers were melt-spun in a range of takeup velocities, and their crystallinity values were quantified by DSC. The thermal behavior of fibers is shown in Figure 7 for DDR of 200. The melting point, T_m, remains nearly unchanged near 160−162 °C for all the samples but the peak of unfilled PP has the narrowest shape. The width of the

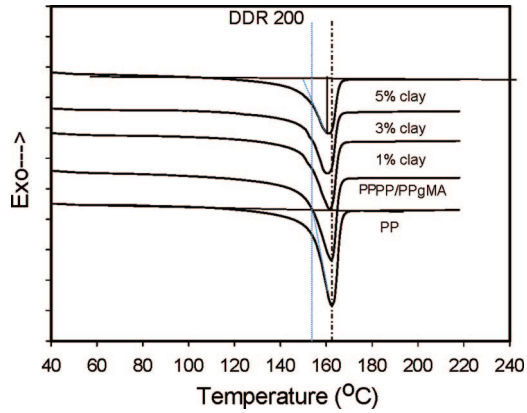

Figure 7. DSC Thermograms of PP and PP nanocomposite fibers produced at 200 DDR.

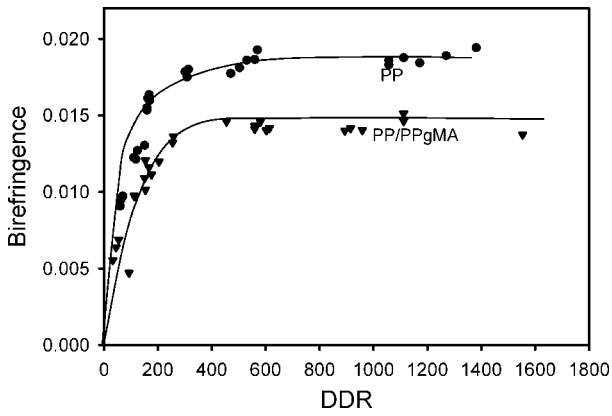

Figure 8. Birefringence vs DDR of PP and PP/PPgMA fibers.

Table 2. Fwhm of Melting Peak of PP and PP/Nanocomposite Fiber (DDR = 200)

sample	fwhm
PP	8.15
PP/PPgMA/clay 1%	9.64
PP/PPgMA/clay 3%	9.82
PP/PPgMA/clay 5%	10.32

Table 3. Crystallinity (%) of PP and PP/Nanocomposite Fiber

DDR	PP	PP/PPgMA	PP/PPgMA/ 1% clay	PP/PPgMA/ 3% clay	PP/PPgMA/ 5% clay
~50	48.9	47.8	48.0	49.3	50.1
~200	50.9	49.1	47.8	49.2	49.8
~1000	52.3	48.6	50.4	51.3	50.3

melting peak is a measure of the crystalline population and size. The full width at half-maximum (fwhm) melting endotherm became broader by the addition of PPgMA and clay (Table 2). The increase in breadth indicates the increase in distribution of crystal size and/or reduction of crystal perfection.

The values of crystallinity of PP, PP/PPgMA, and PP/PPgMA/clay fibers remain unchanged within the experimental error in span from 47−52%, as shown in Table 3. PP/PPgMA shows slightly lower values, and there is a minor tendency to increase crystallinity with deformation in accord with the literature values.[8]

Birefringence of Melt-Spun Fibers. *PP/PPgMA.* The birefringence of the as-spun filaments is plotted as a function of the draw-down ratio (DDR = A_{die}^2/A_{fiber}^2) in Figure 8. Comparison of PP and PP/PPgMA monofilament properties is also necessary because the maleic anhydride-modified polypropylene has lower molecular weight, and thus its presence is expected to modify the orientation behavior of the PP fiber during

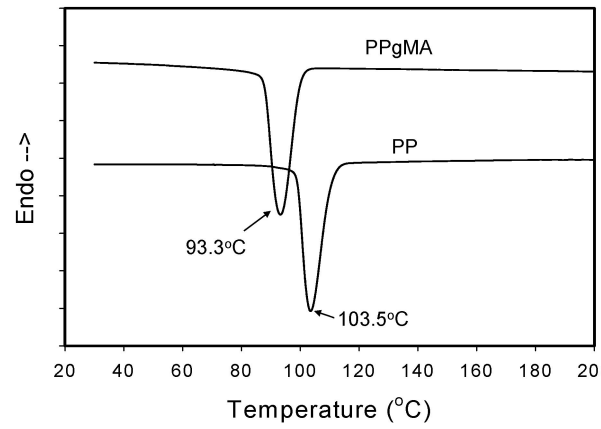

Figure 9. Cooling DSC thermograms of PP and PP/PPgMA.

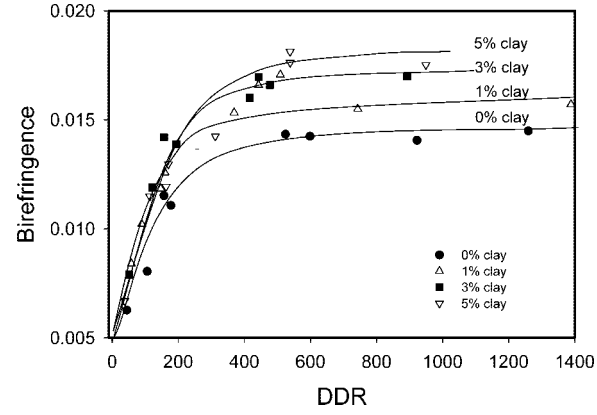

Figure 10. Birefringence vs DDR of PP/PPgMA and PP/PPgMA/clay.

spinning. In this graph, it is evident that the PPgMA reduces the molecular orientation of PP fibers for all spinning conditions employed in this study. Neat PP having higher MW contains an elevated number of entanglements that constrain the polymer chain mobility and consequently results in higher viscosity. The entangled clusters formed between the chains produces a network that acts like physical cross-links and favors the orientation of molecular chains under stress during processing. Addition of low-molecular-weight PPgMA reduces the number of entanglements and favors the relaxation process which takes place during spinning. As a result, the polymer chains in the presence of low-MW PPgMA exhibits lower birefringence than neat polypropylene regardless of deformation conditions employed.

Another reason for obtaining low orientation in PP/PPgMA fibers is attributed to the crystallization behavior of maleic anhydride-modified polypropylene. PPgMA crystallizes at lower temperatures as compared to unmodified PP as shown in Figure 9. This is despite its lower molecular weight that should have had the opposite effect. This means that the molecular modification of maleic anhydride significantly slows down the crystallization process. Therefore, during fiber spinning the chains of PP/PPgMA crystallize at lower temperatures than the chains of neat polypropylene fiber. The delay in crystallization by about 10 °C allows the polymer chains to further relax during the spinning process, resulting in lower levels of orientation.

PP/PPgMA/Clay Nanocomposites. Figure 10 shows that birefringence values of PP/PPgMA and PP/PPgMA/clay fibers increase steadily with the draw down ratio (DDR), and they level off. Birefringence, and hence the total orientation of the fibers, increases with the addition of clay to PP/PPgMA. Similar behavior was observed by Yalcin and Cakmak[25] when they

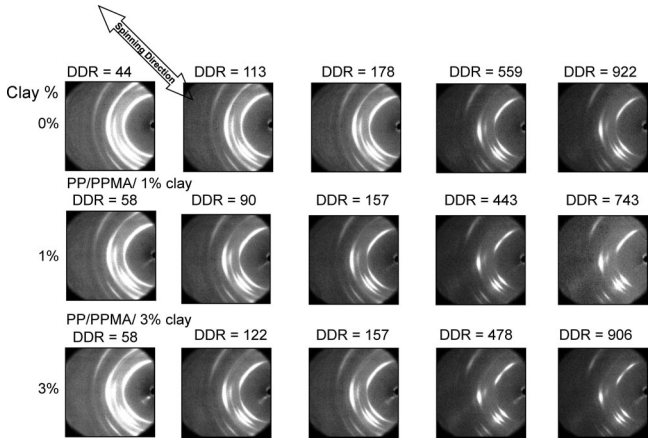

Figure 11. Effect of DDR and clay content on WAXD patterns of PP/PPgMA and PP/PPgMA/clay fibers.

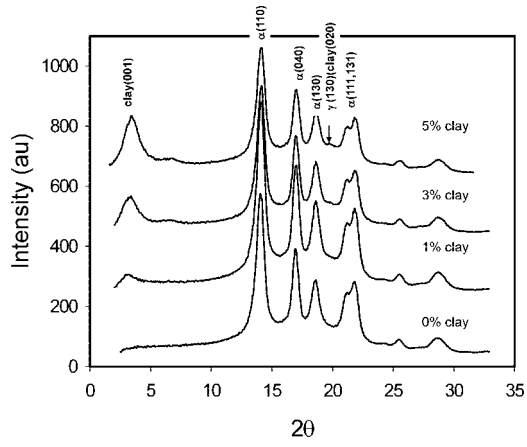

Figure 12. PP/PPgMA and PP/PPgMA/clay fibers at DDR ~ 300.

evaluated the effect of montmorillonite clay loading on the birefringence development during uniaxial stretching of poly(vinyl chloride) films. In their work the incorporation of nanoparticles in PVC promoted the orientation levels significantly for both the crystalline and amorphous phases during the stretching process. The presence of nanoplatelets increases the continuity of the network formed by the amorphous chains/or crystallites in combination with entanglements, and this helps transfer the local stresses to the chains, resulting in higher orientation levels.

Crystalline Orientation. Figure 11 shows WAXD patterns of PP/PPgMA and PP/PPgMA/clay fibers spun at a series of DDR. The arrow in this figure illustrates the spinning direction. All the samples exhibit mostly α crystalline phase typical of PP (Figure 12) with very small possibility of PP gamma phase or clay (020). All samples exhibit *a** orientation as evidenced by the presence of meridional (110) peaks in the WAXD patterns of Figure 11. The orientation factors[28,29] of *c* and *b* axes of PP phase (Figure 13) reach their plateau values around DDR of 200−400 range, and the magnitude of these orientation factors for all clay-containing fibers are quite similar and within a reasonable error band always higher than the unfilled counterparts. For PP/PPgMA fibers at low and medium deformation levels (<400 DDR) the orientation develops gradually in contrast to clay-containing fibers. This initial development of clay orientation that ends in plateau may also involve orientation of the clay particles along the fiber axis discussed in the next section.

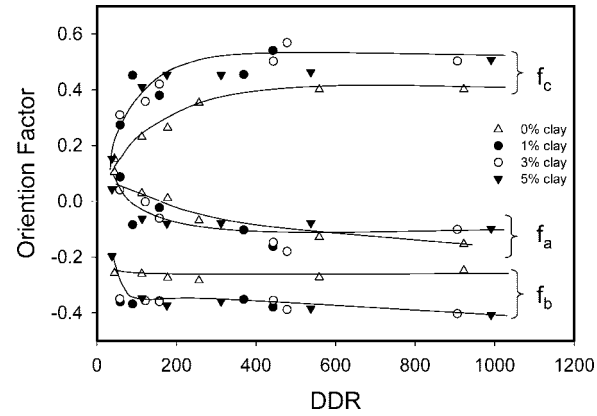

Figure 13. Crystalline orientation factors vs DDR for PP/PPgMA and PP/PPgMA/clay fibers.

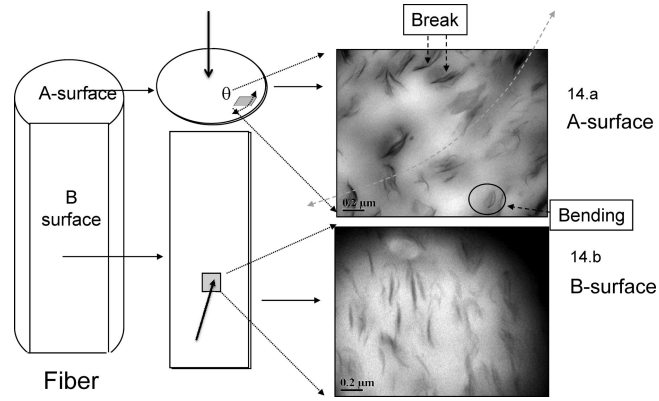

Figure 14. TEM micrographs of PP/PPMA/clay 3% fiber with DDR = 1000: (a) A-surface cut normal to fiber axis; (b) B-surface cut parallel to fiber axis.

Clay Orientation of Fiber under the Influence of Shear and Extensional Forces. In order to assess the clay orientation in the spun fibers, we selected 3 wt % clay-filled PP/PPgMA fiber spun with DDR of 906 and embedded in epoxy to facilitate the cutting process for TEM analysis. These embedded fibers were cryo-sectioned in two planes: one parallel (B-cut) and other perpendicular (A-surface cut) to the fiber axis. Figure 14a presents a micrograph of nanocomposite fiber sectioned perpendicular to the spinning direction close to the original fiber surface. There is a tendency to orient in the θ (hoop) direction in the fibers with the broad surfaces of the nanoparticles becoming parallel to the outer edges of the fibers. In addition, a fair number of these clay particles are bent or exhibit breakage. This is expected as the fibers become thinner there is a lateral contraction as part of the extensional deformation process, and this results in breakage or bending. The break appears to occur on platelets containing multiple layers. Thinner platelets tend to bend. Figure 14b with B-cut surface, sliced as shown in the figure, confirms that the orientation of the clay particles is primarily along the fiber axis. In all pictures, we still observe the presence of intercalated and exfoliated platelets.

In order to assess the overall superstructure of the fibers, the SAXS patterns of samples containing 5% clay were taken for DDR of 38 and 949 (Figure 15). The X-ray beam was directed perpendicular to the fiber axis. The presence of equatorial streak pattern confirms the result of TEM that the nanoplatelets are oriented parallel to fiber axis with some distribution of gap distance between them as indicated by the broadening of the streak. Ergungor et al. also observed this[26] in nylon-6/clay fibers where even at the lowest takeup speeds this alignment was noticed. In their study, the increase in DDR was found to have

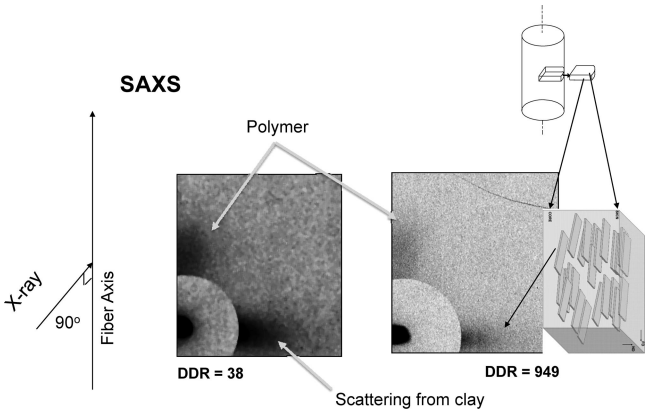

Figure 15. SAXS patterns of PP/PPgMA/5% clay at DDR = 50 (a) and DDR = 1000 (b).

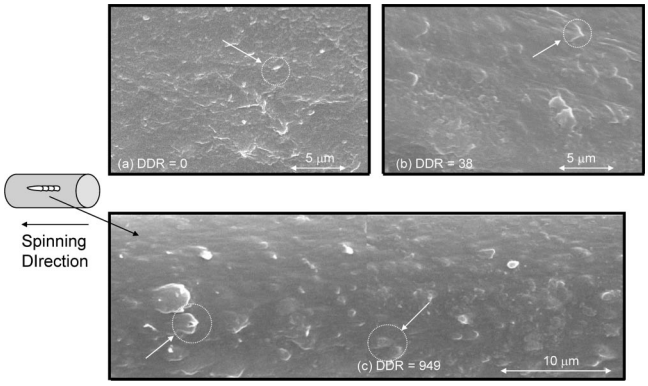

Figure 16. SEM micrographs of PP/PPgMA/clay 5% fibers with different draw ratio.

little to no effect on these orientation behaviors. In our case, the increase in spinning speed substantially reduces the azimuthal spread of the equatorial streak, indicating that the clay particles enhance their alignment along the spinning direction with increasing takeup. In addition, we also observe that the meridional streaklike pattern signifying the presence of long periods (= crystalline lamella + amorphous region) exhibiting a fair amount of long period distribution in the fiber axis direction.

Figure 16 shows SEM micrographs of PP/PPgMA/clay 5 wt % fiber surface at three different draw ratios: 1, 38, and 949. At 1 DDR many of nanoplatelet edges can be observed on the surface of the fiber. To facilitate the analysis, the region surrounded by a circle indicated by an arrow shows appearance of the clay particles on the surface of the samples with some showing an unusual "fish scale" arrangements with the head of the "fish" pointing in the spinning direction. This surface analysis confirms the mechanism of preferential orientation of the nanoplatelet planes parallel to fiber axis with the increase of draw-down ratio.

Birefringence of Nanoplatelets in Fiber. In fiber spinning of PP with high DDR, birefringence increase is mainly due to the extensional forces of the spinning process and concurrent crystallization. In the nanocomposites systems, in addition to the orientation birefringence, one should also consider birefringence contribution due to the presence of nanoplatelets. The monoclinic crystal of montmorillonite has three indices of refraction: $n_\alpha = 1.55$, $n_\beta = 1.57$, and $n_\gamma = 1.57$.[30] Figure 17 shows three possible conformations of montmorillonite with their corresponding contributions to the total birefringence. There is no contribution to the birefringence of the system when the platelets lie with their face parallel to the plane of the fiber

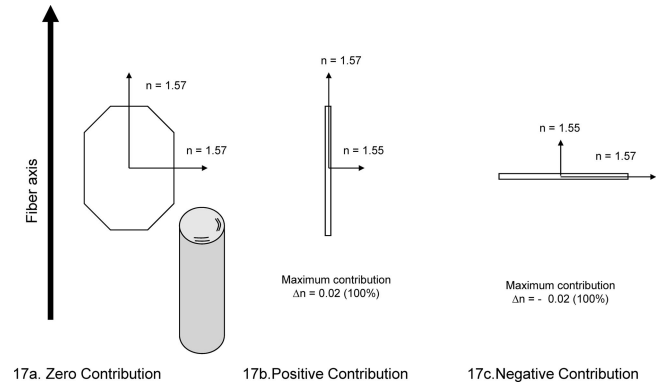

Figure 17. Effect of the clay conformation in the birefringence.

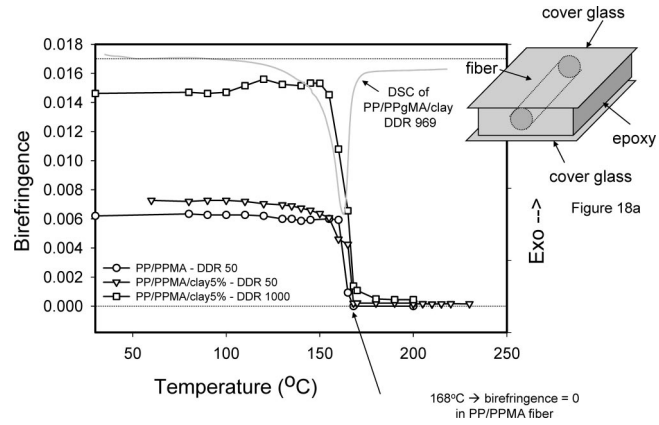

Figure 18. Birefringence development during confined melting of PP/PPMA and PP/PPMA/clay 5% fibers with 50 and 1000 DDR. The DSC curve is also presented to guide the eye.

(Figure 17a). The platelets contribute positively to the birefringence when they orient with their edges parallel to the fiber axis (Figure 17b) and negatively when they align with their edges perpendicular to the fiber axis (Figure 17c).

The birefringence values of the fibers prepared in this study include contributions from not only the polymeric component but also the nanoplatelet fillers. In order to determine the clay contribution in the birefringence, PP/PPgMA and PP/PPgMA/clay fibers with different DDR were embedded in epoxy and taken into two thin glass covers (Figure 18a).

The embedded fibers sandwiched between the two glass covers are placed on a hot stage mounted on a polarizing microscope, and retardation of the sample was measured as a function of temperature by step increase temporal programming of temperature. At each temperature, the sample was kept for 2 min for temperature equilibration prior to retardation measurement. Figure 18b shows birefringence−temperature profiles of three fibers: PP/PPgMA with DDR = 44, PP/PPgMA/clay 5 wt % with DDR = 38 and 949. As the temperature is increased beyond the onset of melting, we observe a slight increase in birefringence. This is most pronounced in the DDR 949 containing 5% clay, presumably signifying some melting and oriented crystallization competing mechanism taking place. When the temperature approaches the peak melting temperature (DSC curve was drawn on this figure to guide the eye), birefringence rapidly declines. The unfilled sample quickly reaches zero birefringence before the end of melting range whereas the nanoparticle filled fibers reach a plateau until about 200 °C. In the latter samples, although the polymer matrix melts away (equilibrium melting temperature of PP is 187.5 °C[31]), the clay particles are prevented from disorienting by confining epoxy, and the plateau values being measured are due to clay

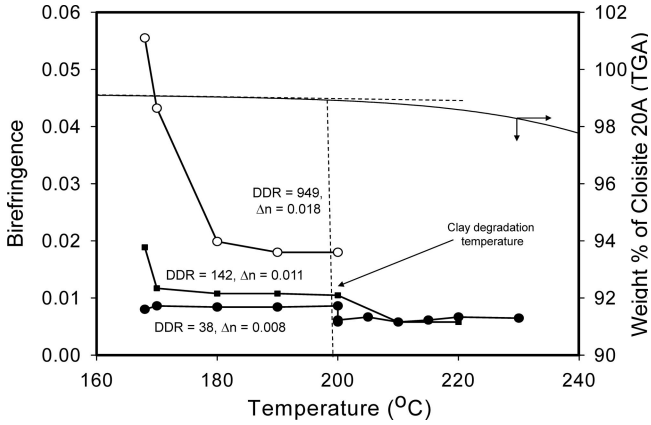

Figure 19. Birefringence of PP/PPMA/clay 5% fibers at 38, 142, and 949 DDR and TGA of Cloisite 20A (in gray).

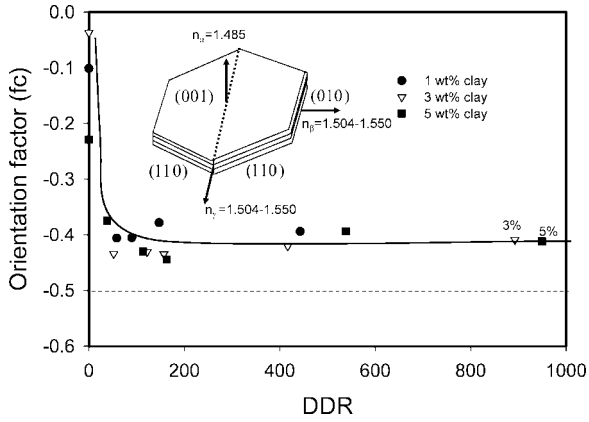

Figure 20. Orientation factor of nanoclay plane (001) in fibers.

Table 4. Amorphous Orientation Factor of 5% Clay Fibers

DDR of PP/PPgMA/ clay 5%	amorphous orientation factor (f_a) $\Delta n = Xf_c\Delta_c^\circ + (1 - X)f_a\Delta_a^\circ + \Delta n_{form}$	amorphous orientation factor (f_a) $\Delta n = Xf_c\Delta_c^\circ + (1 - X)f_a\Delta_a^\circ$	error (%)
38	0.117	0.120	3.1
142	0.205	0.214	4.4
949	0.374	0.389	4.1

particles only. A close-up (Figure 19) of the data above the melting peak temperature clearly illustrates the effect of takeup speed on the plateau birefringence exhibited by the fibers. As the DDR increases so does the plateau birefringence representing preferential orientation of clay platelets along the fiber axis. The organically modified clay undergoes degradation about 200 °C as illustrated by the TGA scan also shown in Figure 19. This explains the secondary decrease of birefringence beyond this degradation temperature in DDR 38 and DDR 142. For DDR 949 the experiment was not carried out beyond the degradation temperature.

Orientation Development in Clay Phase. We decided to investigate the orientation of nanoplatelets by evaluating the azimuthal intensities of (001) peak in the WAXD. Obviously, with this analysis we are assuming that the clay regions with intact crystalline structure approximately represent the orientation of the fully exfoliated clay that should not give rise to such a peak. These orientation factors as a function of DDR are presented in Figure 20 for 1, 3, and 5% clay loadings. At DDR 1 the fiber with higher nanoclay concentration shows higher magnitude in orientation factor (higher negative value) presumably as a result of the shear forces produced by the die wall.

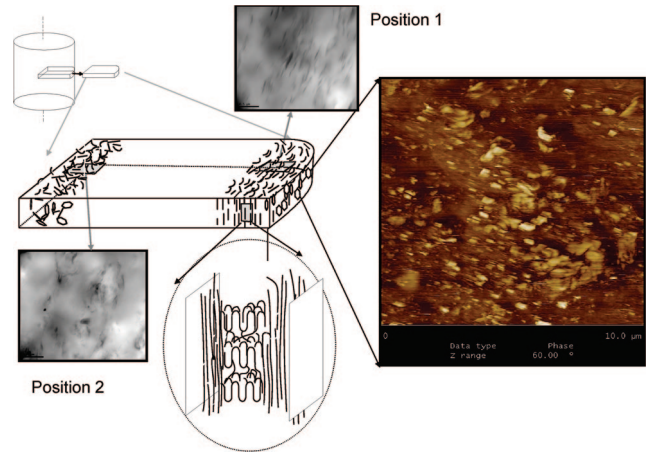

Figure 21. Molecular model of monofilament with no takeup.

With further increase in DDR, the orientation function increases rapidly in all compositions until 50 DDR is reached, and beyond this point it levels off, becoming independent of the draw ratio or clay concentration. Combining these results with the TEM observation, we can conclude that the relatively randomly oriented clay platelets in the interior rapidly align parallel to the spinning direction and beyond a critical value; further increase in the DDR does not change their orientation.

For nanoparticle 5% filled systems, we were able to subtract the birefringence contribution of the clay particles (Δn_{form}) determined in our last experiments and applied the equation $\Delta n = Xf_c\Delta_c^\circ + (1 - X)f_a\Delta_a^\circ + \Delta n_{form}$ to quantify the amorphous orientation factor (f_a) of three fibers (DDR 38, 142, and 949). The results are presented in Table 4, and it is clear that the amorphous phase in the presence of clay reaches higher orientation levels as DDR is increased. For comparison, we also calculate the amorphous orientation factor considering the birefringence contribution of clay insignificant ($\Delta n_{form} = 0$) and the difference between amorphous orientation factors are lower than 5%.

Structural Interpretation. A model for the structure of the nanocomposite monofilaments with zero takeup is shown in Figure 21. The model details the small sections of the fiber where TEM and AFM were performed. We verified that while the clay surfaces are oriented parallel to the skin (position 1), they exhibit nearly random orientation in the core region (position 2). This is due to the shear stresses exerted on the material during its passage through the die. In such a stress field, the nanoplatelets rotate and orient with their broad surfaces parallel to the outer surface. Since there is no strong shear gradient in the core, the nanoplatelets keep their random orientation.

Those chains that are confined in the vicinity of the oriented nanoplatelets undergo disproportionately higher orientation under the shear amplification effect caused by the relative sliding motions of the adjacent clay particles in the shear field. Additionally, because of this rigid confinement effect, the orientation relaxation is substantially reduced, thereby retaining the developed orientation in the final crystallized structure near the skin. However, toward the center of the fiber, clay platelets are randomly oriented. Even though WAXS data suggest random orientation in the PP phase in the core, there may be remnants of oriented chains trapped between the clay particles. They may appear random as guided by the random orientation of the particles. A much finer experimental technique may shed light to this detail in the future.

Upon application of takeup, the polymer chain orientation as well as clay orientation rapidly increase in magnitude and

reach a plateau. There is a clear indication that the presence of nanoparticles accelerates the approach to this plateau at low deformation levels.

Conclusions

The presence of nanoparticles has a profound effect on the radial structure gradient developed in the melt-spun PP/PPgMA blends. TEM analysis on the cross section of the fibers with no takeup indicates preferrential orientation of the broad surfaces of the platelets parallel to the outer skin as a result of shear history experienced in the die. Near the center, these platelets were observed to exhibit random orientation. In parallel with the clay orientation gradient, the polymer chains exhibit similar radial distribution of orientation behavior. This was attributed to the substantial enhancement of orientation of confined chains due to shear amplification between the nanoparticles. This phenomenon combined with substantial decrease of orientation relaxation due to the rigidifying effects of the clay particles yields substantial orientation in these as-spun fibers with no takeup.

We have shown that the oriented clay particles contribute positively to the total birefringence of the fiber as a result of their preferrential orientation.

The polymer chains reach a finite orientation levels at low to moderate takeup speeds in the presence of clay platelets. For that reason by adding a small amount of nanoparticles (1−5%) greater molecular orientation and consequently enhanced mechanical properties can be obtained at low levels of spinning. Further increases in takeup do not yield further orientation. This behavior is very similar to the results observed in thermotropic liquid crystalline polymers and their blends in the literature.[32−34] Remarkably, the presence of clay particles makes the relatively flexible polymers like polypropylene behave very similar to thermotropic liquid crystalline polymers, including ease of orientation at low deformations and substantially reduced chain orientation relaxation.

References and Notes

(1) Ahmed, M. *Polypropylene Fibers—Science and Technology*; Elsevier Scientific Publishing Co.: Amsterdam, 1982.
(2) Katayama, K.; Amano, T.; Nakamura, K. *Kolloid Z. Z. Polym.* **1968**, *226*, 125–134.
(3) Kitao, T.; Ohya, S.; Furukawa, J.; Yamashita, S. *J. Polym. Sci., Polym. Phys. Ed.* **1973**, *11*, 1091–1109.
(4) Shimizu, J.; Shimazaki, K. *Sen'i Gakkaishi* **1973**, *29*, T442–T450.
(5) Ohio, H. C.; White, J. L. *Polym. Eng. Sci.* **2000**, *40*, 645.
(6) Spruiell, J. E.; White, J. L. *Polym. Eng. Sci.* **1975**, *15*, 660.
(7) Ishizuka, O.; Koyama, K. *Sen'i Gakkaishi* **1976**, *22*, T-43.
(8) Nadella, H. P.; Henson, H. M.; Spruiell, J. E.; White, J. L. *J. Appl. Polym. Sci.* **1977**, *21*, 3013.
(9) Nam, P. H.; Maiti, P.; Okamoto, M.; Kotaka, T.; Hasegawa, N.; Usuki, A. *Polymer* **2001**, *42*, 9633.
(10) Kawasami, M.; Hasegawa, N.; Kato, M.; Usuki, A.; Okada, A. *Macromolecules* **1997**, *30*, 3516.
(11) Manias, E.; Touny, A.; Wu, L.; Strawhecker, K.; Lu, B.; Chung, T. C. *Chem. Mater.* **2001**, *13*, 3526.
(12) Maiti, P.; Nam, P. H.; Okamoto, M. *Macromolecules* **2002**, *35*, 2042.
(13) Solomon, M. J.; Almusallam, A. S.; Seedfeldt, K. F.; Somwangthanaroj, A.; Varadan, P. *Macromolecules* **2001**, *34*, 1864.
(14) Hasegawa, N.; Kawasumi, M.; Kato, M.; Usuki, A.; Okada, A. *J. Appl. Polym. Sci.* **1998**, *67*, 87.
(15) Zhang, X.; Yang, M.; Zhao, Y.; Zhang, S.; Dong, X.; Liu, X.; Wang, D.; Xu, D. *J. Appl. Polym. Sci.* **2004**, *92*, 552.
(16) Pavliková, S.; Thomann, R.; Reichert, P.; Mulhaüpt, R.; Marcincin, A.; Borsig, E. *J. Appl. Polym. Sci.* **2003**, *89*, 604.
(17) Mlynarcýkova, Z.; Kaempfer, D.; Thomann, R.; Mülhaupt, R.; Borsig, E.; Marcincin, A. *Polym. Adv. Technol.* **2005**, *16*, 362–369.
(18) Alexander, L. E. *X-ray Diffraction Methods in Polymer Science*; Wiley-Interscience: New York, 1974.
(19) Product Bulletin/Cloisite@20A, Southern Clay Products, Inc., TX (www.scprod.com/product_bulletins/PB%20Cloisite%2020A.pdf).
(20) Stein, R. S.; Norris, F. H. *J. Polym. Sci.* **1956**, *21*, 381.
(21) Samuels, R. J. *J. Polym. Sci.* **1965**, *A3*, 1741.
(22) Quirk, R. P.; Alsamarraie M. A. A.; Brandrup, J.; Immergut E. *Polymer Handbook*, 3rd ed.; Wiley: New York, 1989.
(23) Lee, K. M.; Han, C. D. *Polymer* **2004**, *44*, 4573.
(24) Yalcin, B.; Valladares, D.; Cakmak, M. *Polymer* **2003**, *44*, 6913.
(25) Yalcin, B.; Cakmak, M. *J. Polym. Sci., Part B: Polym. Phys.* **2005**, *43*, 724.
(26) Ergungor, Z.; Cakmak, M.; Batur, C. *Macromol. Symp.* **2002**, *185*, 259.
(27) Hwang, W. R.; Peters, G. W. M.; Hulsen, M. A.; Meijer, H. E. H. *Macromolecules* **2006**, *39*, 8389–8398.
(28) Hermans, P. H. *Contribution to the Physics of Cellulose Fibres; a Study in Sorption, Density, Refractive Power and Orientation*; Elsevier Pub. Co.: Amsterdam, 1946.
(29) Wilchinsky, Z. W. *J. Appl. Phys.* **1960**, *31*, 1969.
(30) *CRC Handbook of Chemistry and Physics*, 81st ed.; Chemical Rubber Company: Boca Raton, FL, 2001.
(31) Brandup, J.; Immergut, E. H.; Grulke, E. A. *Polymer Handbook*, 4th ed.; Wiley: New York, 1999.
(32) Crevecoeur, G.; Groeninckx, G. *Polym. Eng. Sci.* **1990**, *30*, 532–42.
(33) Lin, C. H.; Maeda, M.; Tayebi, A.; Blumstein, A. *Polym. Prepr.* **1989**, *30*, 458–9.
(34) Lee, W. C.; Dibenedetto, A. T.; Gromek, J. M.; Nobile, M. R.; Acierno, D. *Polym. Eng. Sci.* **1993**, *33*, 156–65.

MA8007527